Journal of Tribology. Received November 01, 2024;
Accepted manuscript posted March 18, 2025. doi:10.1115/1.4068245

The Difficulty of Measuring Surface Topography in Additive Manufacturing: A Comparison Between Measured and True Surface Features of Binder-Jet Printed Samples

Authors

Cora Brown[1a], Meg Nescio[1a], Vimanyu Chadha[a], Chuyuan Zheng[a], Esta Abelev[a], Markus Chmielus[a], Tevis D. B. Jacobs[a]*

[1] designates equal co-authorship
* Corresponding author, email: tjacobs@pitt.edu
[a] Department of Mechanical Engineering and Materials Science,
University of Pittsburgh
3700 O'Hara St, Pittsburgh PA 15261, USA

Abstract

Surface topography represents a critical barrier to the advancement of additive manufacturing (AM). Because some internal features cannot be polished, and because of a growing trend of *in situ* process monitoring, it is important to understand the as-built surface topography of AM components. Here we highlight the challenges of using industry-standard surface-measurement techniques on binder-jet-printed parts. We measured the topography of binder-jet-printed Inconel Alloy 625 samples in their green state and over the course of sintering; this system allowed the investigation of identical starting materials undergoing systematic changes in topography. Specifically, we compared the results from industry-standard surface-measurement techniques—optical interferometry, 3D microscopy (by fringe projection), and stylus profilometry—against the "true topography," as revealed by cross-section scanning electron microscopy. While the true topography changed significantly with sintering, the industry-standard techniques detected no change in root-mean-square height because of complex surface features, including multi-scale topography, overhangs, and steep surface slopes. While these findings do not invalidate the use of industry-standard techniques for binder-jet-printed samples, they demonstrate a challenge in their application, and they motivate the development of new metrics and new techniques to more accurately describe surface topography in AM.

Keywords- Scanning electron microscopy; Inconel alloy 625; binder jetting; 3D printing

Journal of Tribology. Received November 01, 2024;
Accepted manuscript posted March 18, 2025. doi:10.1115/1.4068245

INTRODUCTION

Reports by the National Science Foundation (NSF) [1] and the National Institute of Standards and Technology (NIST) [2] underscore the fact that surface topography represents a critical barrier to the advancement of AM. 3D printing, or AM, has found applications from aerospace [3] to medicine [4], and has demonstrated the unique advantage of being able to create complex features, such as lattice structures for lightweighting, or scaffolds for cell growth, or heat exchangers, all of which have internal surface features [3]. However, a key challenge of additive manufactured structures is their rough and complex surface topography, which degrades performance in terms of fatigue life [5,6], fluid flow [7], and biocompatibility [8]. Recent work indicates that the surface of these AM materials is quite distinct from those of traditionally manufactured surfaces, both because of higher complexity of the engineered part (i.e. its form) and because unique surface textures frustrate attempts to establish repeatability and traceability [9]. Prior research by Leach and co-workers [10] demonstrate large discrepancies across characterization technologies, and identify the lack of a protocol for obtaining an accurate "ground truth" to evaluate these methods. Cross-section scanning electron microscopy (SEM) is a potential candidate for establishing such ground truth [11], but has not yet been applied to AM parts for this purpose. Additionally, there is a lack of research on non-beam-based AM technologies such as binder jet printing.

The as-built surface topography of 3D-printed parts is important to understand and control. First, while it is true that the majority of AM components will be subjected to a post-printing surface-finishing process (grinding, polishing, honing, etc.) that modifies the external topography, many AM components are designed with internal features and channels, which cannot easily be polished or otherwise finished. Even flow-through techniques for surface finishing, such as abrasive flow machining [12], have difficulty yielding consistent properties for complex internal features. Therefore, it is important to be able to predict and control as-built topography. Second, an emerging trend in additive manufacturing is the *in situ* measurement of the morphology of a part during the printing process. This allows the measurement of internal and external dimensions of the product, and real-time process monitoring for surface defects [13,14]. These have been shown to improve the overall quality and tolerances of AM parts, and to help prevent unexpected failures in the part build and structure. However, any *in situ* techniques will necessarily only have access to the as-built topography. For these two reasons, this research focuses on the topography without additional surface finishing.

Some prior research has explored the problem of surface topography in AM; especially on correlating roughness metrics to print conditions and to part performance. Cabanettes *et al.* [15] performed a topography analysis of AM surfaces, analyzing variations from net shape (form) to small-scale features (roughness). Jamiolahmadi and Barari [16] modeled surface topography using a finite difference approach, highlighting the impact of the layer-wise deposition on roughness. Townsend *et al.* [17] reviewed metrology techniques for evaluating AM surfaces, emphasizing the need for standardized characterization methods. Specifically on fluid flow, the topography of additively manufactured microchannels was shown to affect the friction factor of the surface, modifying flow rate and heat transfer, as compared to smooth coupons [18]. Furthermore, the different build directions have been shown to produce varying surface topography, requiring

higher tolerances in some areas and resulting in spatially varying functional performance [19]. Because of its effect on surface function [20], surface topography can be intentionally modified to optimize the performance of manufactured parts [21]. More Specifically, for binder-jet-printed samples, Mostafaei *et al.* [22] correlated surface finish to fatigue behavior in binder-jet printed Inconel 625. Atapour *et al.* [23] explored how surface finishing impacts the corrosion resistance of binder-jet 316L stainless steel. Lores *et al.* [24] investigated process-parameter optimization and post-processing to improve surface quality in binder-jetted parts composed of Invar36 alloy. Vu *et al.* [25] examined the effects of surface topography and surface area on the performance of 3D-printed scaffolds, showing functional implications of surface design for biomedical applications. Together, these studies underline the importance of understanding and optimizing surface properties to improve performance across AM applications.

While the above investigations have usefully explored the topography of 3D-printed surfaces using conventional, industry-standard techniques, the field lacks sufficient investigation of whether these industry-standard techniques are capable of accurately capturing the complex topography of AM parts. This is relevant because the performance of AM parts depends on their *true* topography and thus will have only an indirect dependence on the less-accurately *measured* topography. For example, the fatigue life of an aerospace component may depend on the true topography because the deepest and sharpest features act as stress concentrators. However, if these features are not accurately captured due to resolution limits of surface-measurement techniques, then fatigue life may show only a weak correlation with measured topography.

The purpose of this investigation is to compare the true topography of binder-jet 3D-printed surfaces against their measured topography using industry-standard techniques—stylus profilometry, 3D optical microscopy (fringe projection), and scanning white-light interferometry. We use all three industry-standard techniques to measure the topography of binder-jet printed parts in various stages of sintering; then we perform a cross-section examination using scanning electron microscopy to assess the true topography of the part. The differences between them are, as a function of sintering time, represented by comparing the line profiles of measured topographies, and also by computing the root-mean-square height variation.

METHODS

Samples were created using binder-jet printing with various levels of sintering and densification, and therefore different sizes and types of surface features. Binder-jetting provides an ideal platform for achieving controllable and predictable changes in density and topography of an AM part. Specifically, a part can be measured at all stages from “green” (just after binder-jetting) to fully fused – instead of only having access to the post-fusion part as would be typical for energy-beam-based AM. Also, because the sintering process involves material diffusion at high temperature, changes in topography can be evaluated in the context of simple diffusion equations.

Sample Printing and Sintering

Parts with a near-cubic shape (Fig. 1), and dimensions of 10 x 10 x 13 mm^3, were printed using nitrogen-atomized Inconel 625 powders with a particle size distribution of 16-63 μm. Additional

Journal of Tribology. Received November 01, 2024;
Accepted manuscript posted March 18, 2025. doi:10.1115/1.4068245

fabrication details can be found in Ref. [26]; the coordinate axes were defined relative to the print directions. The samples then went through the sintering process at a super-solidus temperature of 1285 °C. The sintering was performed in a Lindberg tube furnace for six durations, 0 h, 0.25 h, 0.5 h, 0.7 h, 1.0 h, and 1.5 h [26–28]. The "0 h" sample was brought up to temperature, then cooled back down immediately, thus spending approximately zero time at a super-solidus temperature. The rest of the samples were held at the super-solidus temperature for their respective times before controlled cooling. A green sample (unsintered, designated GS) was also tested as a reference, as well as a sample brought up 1270 °C then cooled immediately back down, designated the solid-state-sintered (SS) sample.

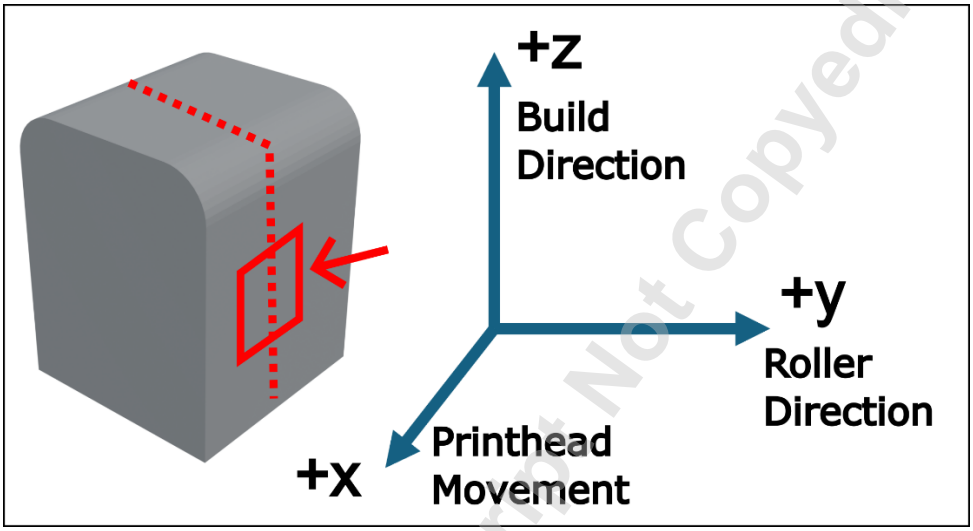

Figure 1: Schematic drawing of the ~1 cm cube sample, showing the relevant axes: printhead movement is along the x-axis, the roller direction is along the y-axis, and the build direction is along the z-axis. The industry-standard techniques were performed on the y-face (red square), which is the plane containing both the build direction and the printhead movement. The red dotted line indicates the plane along which the sample was cross-sectioned. The SEM imaging was performed in the same location and orientation of the y-face (indicated by a red arrow) to ensure registry across all measurements.

Industry-standard Techniques for Topography Measurement

Three techniques were chosen for assessment: stylus profilometry, 3D microscopy, and scanning white-light optical profilometry. While many techniques exist to characterize topography, each with their own advantages and disadvantages, the authors believe these are the most widely used techniques in industrial manufacturing and also in *in situ* process monitoring.

Stylus profilometry (Alfastep IQ, KLA-Tencor, Milpitas, CA) was used to measure each sample in 9 locations, with scan sizes of 300 μm, 1500 μm, and 7500 μm, taken with a data-collection interval of 10, 50, and 200 nm, respectively. Stylus profilometry works by dragging a sharp needle across the surface. As the tip follows the surface contours, the vertical displacement is tracked as a function of lateral position to create a profile. It is well-known that the tip-radius of the needle causes artifacts, where the smallest features are not detected, and the tip cannot fit accurately into

Journal of Tribology. Received November 01, 2024;
Accepted manuscript posted March 18, 2025. doi:10.1115/1.4068245

deep valleys, causing characteristic downward "kinks" in the data [29–31]. In the present work, a 5-μm diamond tip was used.

3D microscopy (via fringe projection) was also performed, using a 3D digital microscope (VR-3200 Keyence, Itasca, Illinois). In this technique, which is also called "structured illumination", a pattern of lines is projected onto the sample surface. By measuring how the pattern is distorted by the surface of the sample, the surface topography can be computed [32]. By repeating this process many times, with different-size gratings projected at different angles, a 3D height map of the surface can be computed. Nine measurements were performed of each sample in different locations, with magnifications of 38x, 80x, and 160x. The lowest-mag image has a sample-size of 9000 μm and a pixel size of 9 μm. For the middle- and high-magnification images, the values for (sample size, pixel size) are as follows: (4000 μm, 4 μm) and (2000 μm, 2 μm), respectively.

Scanning white-light interferometry (Contour GT-I, Bruker, Billerica Massachusetts) was also performed. Again, 9 measurements were taken per sample, in different locations with 2.5x, 10x, and 50x objectives. For the low-, middle- and high-magnification images, the values for (sample size, pixel size) are as follows: (1000 μm, 750 nm), (500 μm, 400 nm), and (100 μm, 80 nm), respectively. In this technique, white light is separated by a beam splitter into a reference and a measurement beam which travel to a reference plane and the sample, respectively. The sample beam is reflected and interferes, constructively or destructively, with the reference beam. By scanning vertically over the sample and examining the coherence envelope of the different component colors, the height can be determined for each measured pixel. This procedure is used to build a 3D profile of the surface [33].

"True Topography" as Characterized using Cross-section Scanning Electron Microscopy

To establish the true topography of the surface, a cross-section of the sample was created using metallographic sample preparation and examined using scanning electron microscopy. SEM images were captured at three different magnifications: 500x, 1000x, and 5000x, all along the y-face of each sample. The sizes of these images were 600, 300, and 50 μm, respectively. Each image was captured with 1024 pixels in the horizontal direction; therefore, the pixel sizes of the images were 600, 300, and 50 nm, respectively. The topography was extracted using manual point-selection (using custom MATLAB scripts) that enables an expert user to define the outer contour of the part, recording the profile as a series of coordinates. The use of manual tracing by an expert is time-consuming, but is very well-established (as described for SEM in Refs. [11,34] and for TEM in Refs. [35–37], among others). Furthermore, it is the most robust and reliable way of establishing topography from electron-microscopy images. While computer-vision and edge-finding routines work extremely well in some cases, they must be retrained or reparametrized for each type of measurement (material, microscope, magnification) and are therefore less reliable for smaller sample sizes such as this investigation. The present process (cross-section SEM with manual tracing) is far too slow to be an industry-applicable technique; it is used here for establishing a benchmark of the true surface topography. Once measured, the resulting line profiles can be analyzed in the same fashion as a stylus measurement, or any other topographic line profile, to compute topography metrics.

Journal of Tribology. Received November 01, 2024;
Accepted manuscript posted March 18, 2025. doi:10.1115/1.4068245

RESULTS & DISCUSSION

Figure 2 shows representative images from each of the three industry-standard techniques, showing the real-space height maps at different sintering times. The images show that the topography did not appear to vary significantly with sintering time, which is shown qualitatively by the appearance of the images, and quantitatively by the range of height data observed.

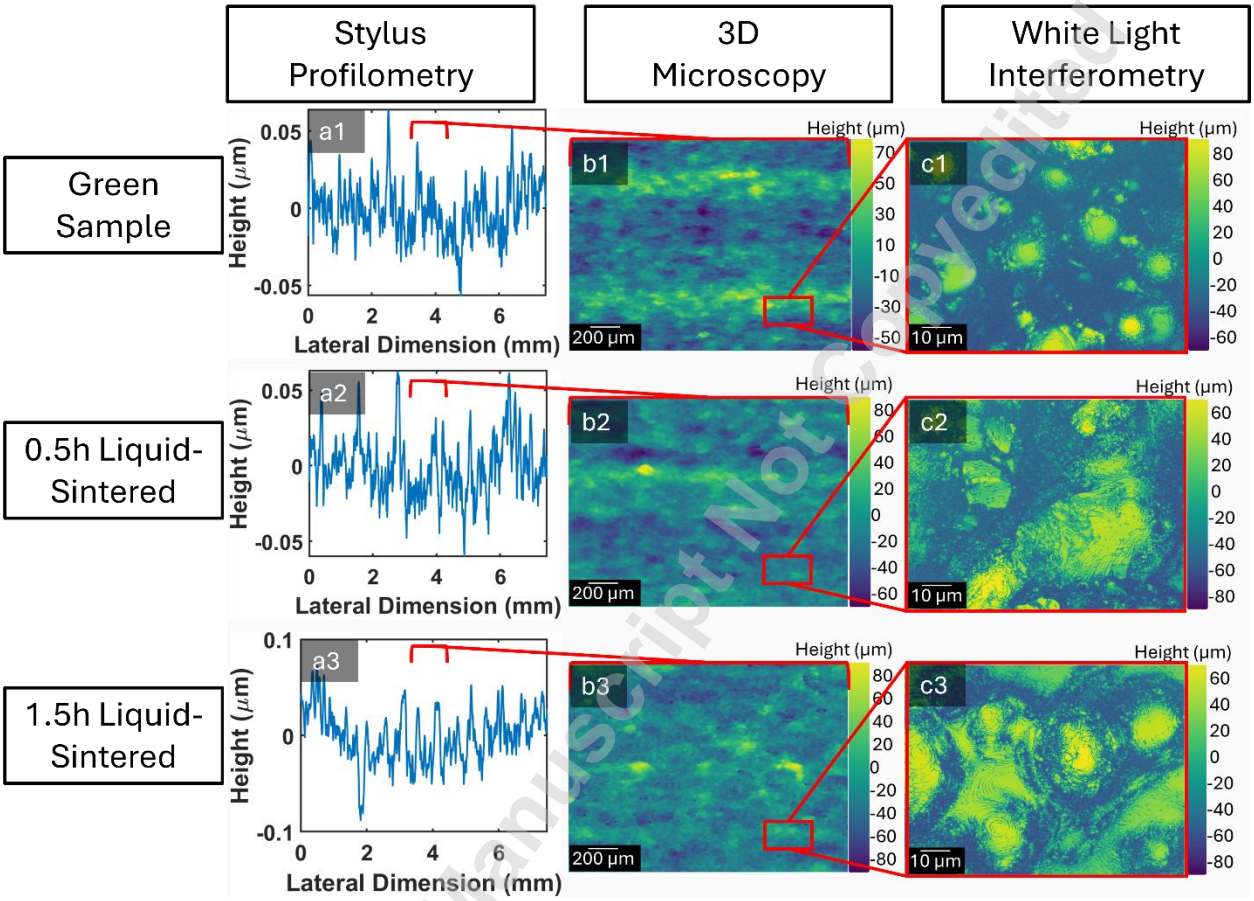

Figure 2. Representative real-space measurements taken on the y-face using (a) stylus profilometry (b) 3D microscopy, and (c) scanning white-light interferometry. Images are shown for (1) the unsintered green sample, and after (2) 0.5h and (3) 1.5h of liquid-state sintering. The leader lines indicate the increases in resolution/scan-size across techniques but are not intended to represent identical locations. The image sizes shown here for Panels a, b, and c are 7500, 2000, and 100 μm, respectively. These were chosen for visual clarity; all raw topography data for all techniques are available as described in Data Availability.

To compute quantitative changes in surface topography, the unfiltered RMS height was computed and compared across conditions and techniques, using the following equation [34]:

$$h_{rms}^2 = \frac{1}{L}\int_0^L h(x)^2 dx \quad (1)$$

Journal of Tribology. Received November 01, 2024;
Accepted manuscript posted March 18, 2025. doi:10.1115/1.4068245

All calculations in the present investigation were performed using the open-source, freely available web application CONTACT.ENGINEERING, which is available at https://contact.engineering and is described in Ref. [38]. Of course, a wide variety of computational software or surface-analysis programs could also have been used to compute the same values. The surface topography measurements were detrended to remove specimen tilt and artificial curvature from the tool by subtracting the second-order polynomial. Also, a reliability cut-off (described in Ref. [39]) was implemented to remove tip-radius artifacts. For non-tip-based techniques, an estimate of resolution was provided by the instrument and all data beyond that resolution limit was removed.

We note that there are many different metrics for describing topography (as defined in international standards [40,41]); as well as many different multi-scale descriptors, such as the power spectral density [42]. Here we chose to use the *unfiltered* RMS height for all instruments. This value would be analogous to the value P_q in international standards. The rationale for this choice is three-fold: (1) the unfiltered RMS height can be numerically computed (using Eq. 1, and as described in Ref. [38]), this renders the analysis easily duplicatable by other researchers; (2) the unfiltered RMS height enables comparison across instruments and scan sizes, and avoids the (somewhat arbitrary) choice of filter size; (3) finally, this value avoids the need to make (also arbitrary) choices of which texture parameter to use and which software implementation to use. Because all data is freely available (see Data Availability), other metrics can be easily applied in future re-analysis.

Figure 3 shows the results for RMS height from the three different conventional tools (stylus profilometry, 3D microscopy, and scanning white-light interferometry). The mean RMS height of all data was 13.87 ± 2.20 µm, with no consistent trend with sintering time. Applying a statistical t-test on the slope of the regression line, we can say that the slope of the best-fit line is not statistically significantly different from zero for any of the three techniques. This result is consistent whether the GS and SS samples are included in the fit (when they are set to x-values of 0, the t (6) = 0.08, the p-value is 0.916) or whether they are excluded from consideration (then the t (6) = 0.75, p-value is 0.793).

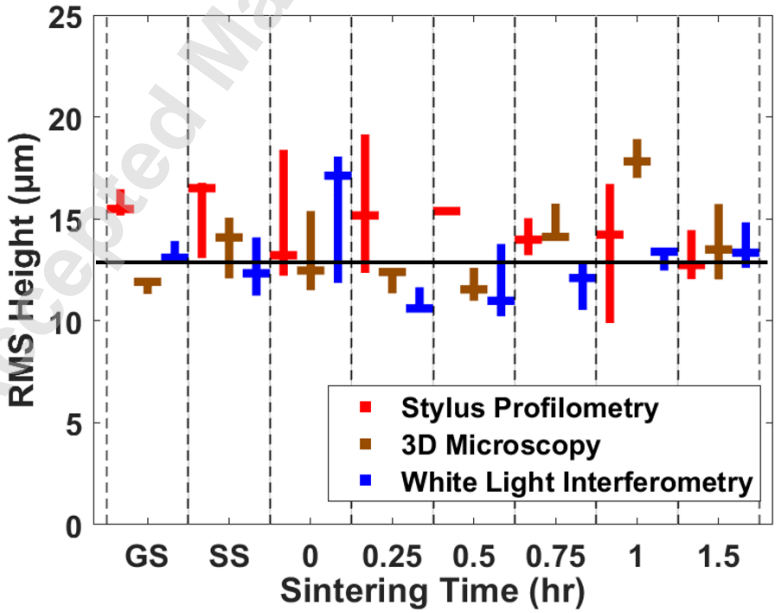

Figure 3: Three industry-standard techniques are incapable of detecting changes in RMS height of additively manufactured samples as a function of sintering time. The GS and SS samples are placed as categorical values, arbitrarily located with respect to x-axis. Within each technique, all values for all magnifications are analyzed together to create each data point, as there were no consistent trends with magnification in any of the industry-standard techniques. A best-fit to all data reveals a constant value of RMS height. A best-fit trend-line reveals no statistically significant change in topography with sintering time, when measuring with these techniques.

While different scan sizes and pixel sizes were used (see Methods), there were no consistent trends in RMS height with magnification or scan size when using conventional techniques. While image stitching could have increased the size of the smallest (interferometry) measurements; this was not used here in order to be representative of how the technique is most commonly applied in real-world manufacturing. Additionally, the ranges of scan sizes for all techniques were sufficiently close to overlapping in scan sizes (stylus at ≥300 μm; 3D microscopy at ≥2000 μm; interferometry at ≥100 μm; and SEM at ≤100 μm) that differences in RMS height cannot simply be attributed to changes in scan size. The constant topography measurement persisted even despite the well-known material changes that occur during sintering [26,43].

To extract the true topography across the sintering period, cross-section samples were created and imaged using SEM. Metallographic measurements were performed in three different locations on each sample, with magnifications and image/pixel sizes as indicated in the Methods. Representative images for each sintering time are shown in Fig. 4, along with the line-tracing method that was used to extract the height profile. Once extracted, the line profiles had scan lengths (lateral dimensions) of 580 μm, 280 μm, and 58 μm. While the graph of the topography (Fig. 4g) may appear distorted from the raw image (Fig. 4f), this is only due to the expansion of the height scale for clarity. This asymmetric zooming is common practice in presenting topography data, see for example Fig. 2a and other standard representations of stylus-profilometer data. Once extracted, the coordinates are then used to calculate the RMS heights to understand the real trends in topography.

Journal of Tribology. Received November 01, 2024;
Accepted manuscript posted March 18, 2025. doi:10.1115/1.4068245

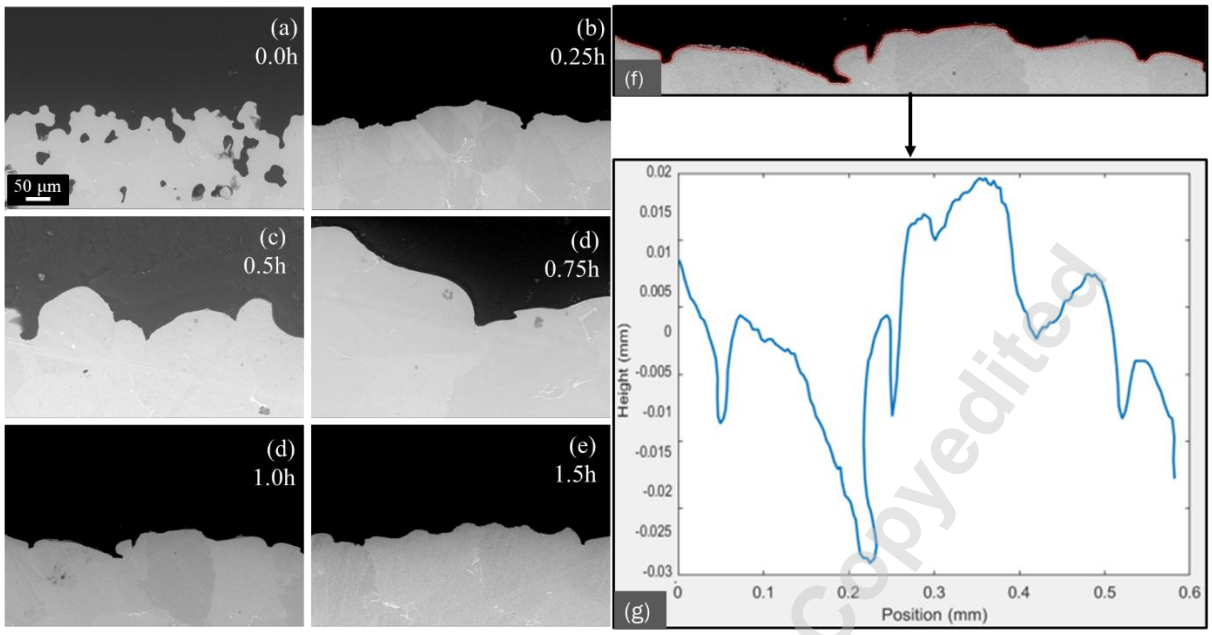

Figure 4: Panels a-e show the cross-sections of the surface as measured in the SEM, with the profiles evolving during sintering time. The 0 h sample shows high porosity and large peak-to-valley variations. The sintering process results in reductions in the small-scale topography, but the natural variability of the large-scale features is unaffected. Panels f and g show the tracing of the 1.0 h profile and its plotting as a height profile.

To quantitatively evaluate the SEM images, the unfiltered RMS height was computed from the line profiles, following the same calculations used for conventional measurements. The results are shown in Figure 5. In this plot, there is a general decreasing trend of topography with sintering time. While there is an increased topography at 1 h, this may be an outlier because the 1.5-hour-sintered sample continues the overall decreasing trend. It should be noted that the lower-magnification SEM measurements show larger values of RMS height, while the higher-magnification measurements produce smaller values. This well-known phenomenon arises because higher-resolution imaging captures only a smaller portion of the material and therefore cannot fully sample the peaks and valleys. This is readily observable in Fig. 4g; if only the central 60 µm were sampled, the RMS deviation (Eq. 1) would be considerably smaller than the same calculation for sampling over the whole 0.6-mm plot. This trend saturates once the measurements are sufficiently large and thus are not observed in the measurements with industry-standard techniques (Fig. 2). Additionally, the SEM can go to sufficiently low magnification that it is able to sample the large-scale topography that is captured using other techniques.

Journal of Tribology. Received November 01, 2024;
Accepted manuscript posted March 18, 2025. doi:10.1115/1.4068245

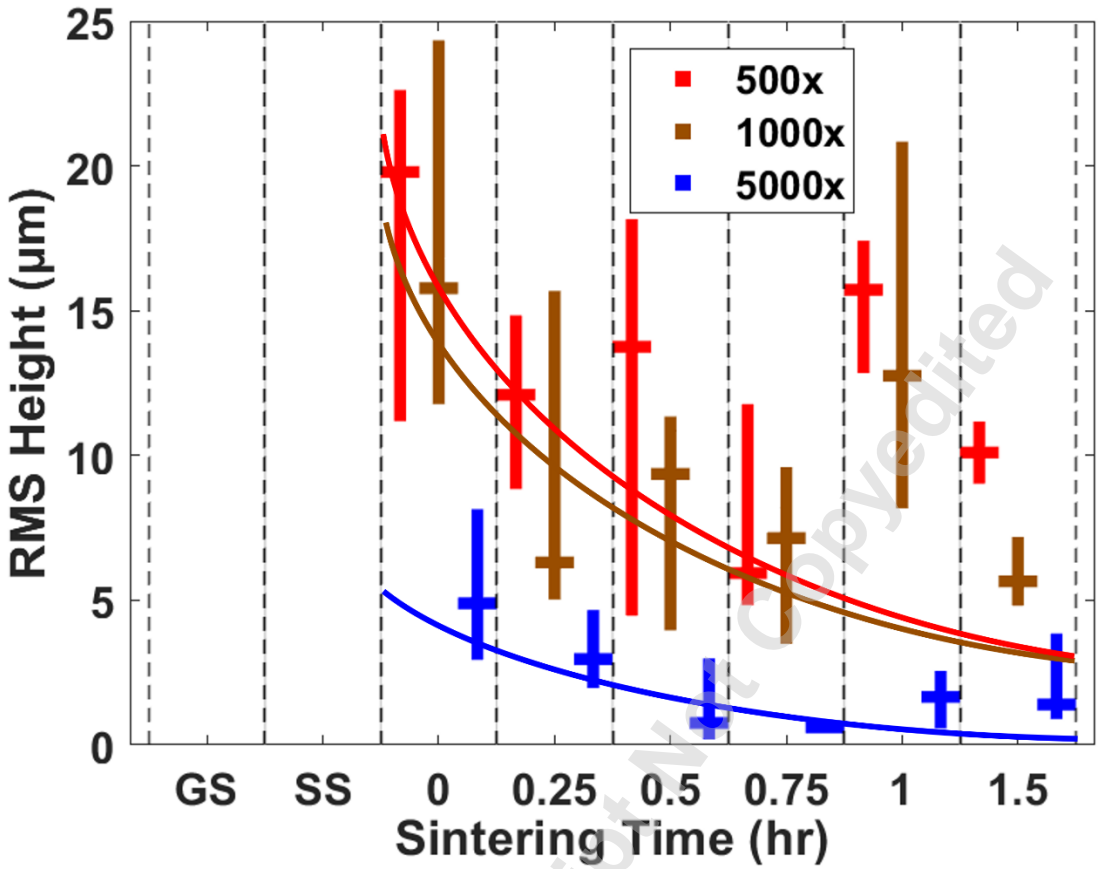

Figure 5: The unfiltered RMS height of the true (SEM-measured) topography is shown as a function of sintering time. Each point represents an average of all measurements at a given magnification. The error bars represent the standard deviation. The curves are best-fit motivated by a simple diffusion equation (Eq. 2).

The SEM measurements reveal an overall decrease in the variation of the true topography with time, which is consistent with the overall kinetics of sintering. At elevated temperature, diffusion enables a curvature-driven smoothening of a curvy profile. The rate of decay of the amplitude will depend on time t and the initial amplitude A(0) according to [44]:

$$A(t) = A(0) \cdot \exp\left(-{}^{\beta t}/_{\tau}\right) \tag{2}$$

where β is a constant proportional to surface diffusivity and surface free energy. For a sinusoidal profile with wavelength λ, the constant τ is proportional to λ^4 [30]. It is well-established that surface topography can be described as the superposition of sinewaves, for instance using the power spectral density [42]. Therefore, Eq. 2 can in principle be applied as a superposition over all wavelengths and all amplitudes A(λ). Because the RMS height is most sensitive to the larger wavelengths, Eq. 2 can be fit to the data shown in Fig. 3 and Fig. 5, with β as the fitting parameter. The characteristic wavelength of all techniques can be approximated as the scan size.

Journal of Tribology. Received November 01, 2024;
Accepted manuscript posted March 18, 2025. doi:10.1115/1.4068245

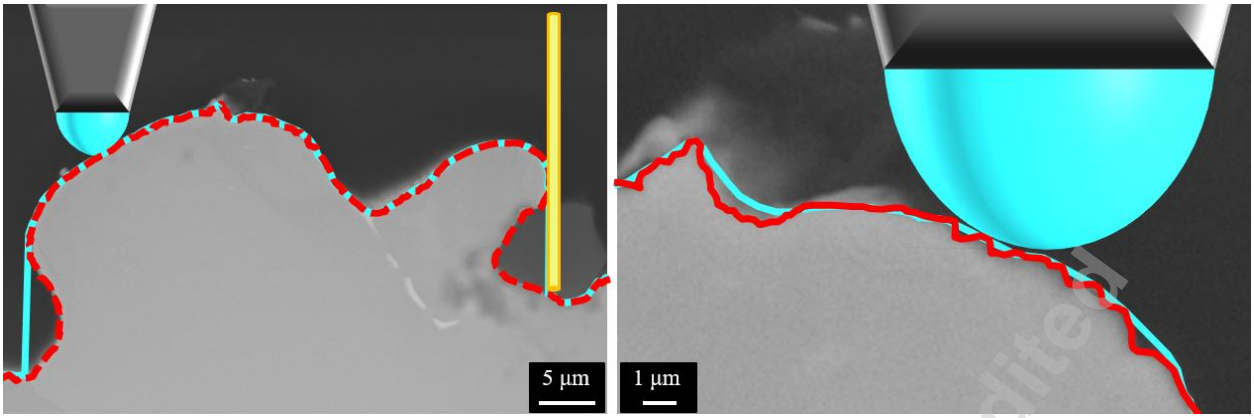

Figure 6: Diagram of how the industry-standard methods are limited and cannot accurately measure the true surface, with their measured contours in blue and the extracted "true" profile shown in red. The left image shows a stylus tip with a radius of 5 µm and a beam of light with a radius of 1 micron, and how they cannot measure overhangs and cavities. The right image shows how there are small-scale features that exist, which conventional techniques cannot sample.

There are two contributions to the discrepancy between true topography and measured topography when industry-standard techniques are applied to AM surfaces. First, the local surface slopes of AM samples are particularly large, with far more overhangs, deep trenches, and near-vertical slopes (Fig. 6) as compared to conventionally manufactured surfaces. These ultra-steep (or negative) slopes cannot be captured accurately by any conventional techniques. The stylus tip comes down from the top with a pyramidal shape. There is a well-documented tip-radius artifact, where topography at or below the scale of the tip radius cannot be accurately sampled; for a typical stylus needle, this tip radius is of order 2-5 µm, and the conical shank of the stylus will make this problem even worse. These artifacts become yet more pronounced on rougher surfaces as compared to smoother [42]. Likewise, the light used in optical techniques is projected downward from the top and will not reflect back from high-angle surfaces. The resolution of optical techniques is also limited, at best by the diffusion limit of light, but is more commonly limited by the lens configuration and can be approximated in the range of single-digit µm. These resolution limits and maximum-local-slope limits mean that stylus and optical techniques work well for surfaces with root-mean-square slopes near zero but are especially poorly suited to characterize surfaces with large values of local slope. Indeed, for the 0-hr-sintered sample, the conventionally measured topography was erroneously low, near 13 µm (Figure 3, 0 hr), while the true measurements showed topography variations closer to 20 µm (Figure 5, 0 hr). In summary, because of ultra-high slopes, industry-standard metrology applied to 3D-printed components has been shown to underreport larger-scale surface topography.

The second way that AM surfaces frustrate industry-standard techniques arises from their intensely multiscale topography. Conventional roughness metrics (including the RMS height, used here, as well as filtered parameters, such as R_a and R_z) focus on a single scale of topography that is defined either by the measurement size or the filter size. While these single-scale parameters can be quite useful in conventional manufacturing, where there is extensive documentation and prior history

characterizing them for different surface-finishing techniques, they are more limited for use on AM parts. As-printed AM samples have contributions to topography that vary widely with lateral scale. The particle size of the powder leaves a signature (as does the hatch spacing, and the melt-pool size in direct-energy-deposition printing) which contributes topographic variation on the scale of 100+ μm. At the same time, the local thermal history of the part (due to sintering or melt-freeze kinetics, depending on printing type) contributes significant topography variation that manifests on many smaller scales, ranging from approximately 100 μm down to the sub-micron scale). Because the kinetics of material transport are size dependent, then the largest-scale topography can be maintained, even while there are significant changes in smaller-scale topography. Qualitatively, this can be observed in the SEM images, where a large stylus tip would measure the topography of the surface in Fig. 4a as being similar to the topography shown in Fig. 4e – despite clear and significant changes in smaller-scale topography. Quantitatively, this can be observed by comparing the time-independent topography measured with conventional techniques (Fig. 3) against the time-dependent topography measured with SEM (Fig. 5). AM surfaces contain significant contributions to topography from large size scales *and* from small size scales; these different scales of topography were relatively uncorrelated in this study, because diffusion-limited mass transport enabled drastic topography changes on the smaller scales, but not the larger scales. Stylus and optical techniques are strongly affected by larger-scale topography, such that important changes in smaller-scale topography cannot be observed. In summary, because of the intensely multi-scale nature of the surface topography, industry-standard metrology applied to 3D-printed components has been shown to overreport small-scale surface topography because it cannot distinguish this from the larger-scale topography described above.

For conventionally manufactured samples, the larger-scale "waviness" [40,41] can be filtered out, leaving behind the small-scale "roughness", which is reasonably well defined for a specific manufacturing process. By contrast, AM surfaces have substantial and multi-scale topography, even in the so-called "roughness" regime, such that the larger-scale "roughness" overwhelms the smaller-scale "roughness". Therefore, any single scalar topography parameter is likely to have limited utility in distinguishing different AM surfaces.

The limitations of the present study include that samples were made using only binder-jet printing, and it is known that topography will vary depending on the specific 3D-printing technique that is chosen. However, because of similarities in the overall character of topography across AM techniques—typically with large variations and a highly multiscale nature—the present insights may generalize to other 3D-printing techniques. Further investigation would be required to validate this link. Another limitation was the use of a single material, Inconel Alloy 625; other materials could be tested to determine whether these insights generalize across metals. Finally, the use of RMS height as the primary comparison metric (see above for rationale of this choice) has advantages in terms of generalizability but does not enable concrete statements about how other surface metrics would or would not vary. All data is freely available (see Data Availability) for download and reanalysis, such that other surface metrics could be tested in future work.

The primary implication of this investigation is that new metrics and new approaches are needed to evaluate the surface finish of additively manufactured parts. Stylus and optical techniques must

be used with caution; they are inadequate to capture the complex surface features associated with AM and can therefore yield misleading values for scalar roughness metrics. This work does not suggest using cross-section SEM in manufacturing, as the technique is prohibitively slow, but rather demonstrates the shortcomings of industry-standard approaches and motivates the search for new techniques and/or metrics. Additionally, for researchers in the fields of surface science or metrology, this investigation further motivates the urgent need to better understand the formation of surface topography in AM, and its effect on 3D-printed parts.

CONCLUSIONS

This investigation assesses the ability of industry-standard surface characterization to measure the topography of additively manufactured samples of Inconel 625. Three key insights emerged.

1. The true topography of the as-printed parts was measured with SEM imaging at various points during sintering. The surfaces became smoother over the sintering time, as characterized with the root-mean-square height, which is well-fit using a simple diffusion-based equation.
2. However, when the same samples were measured using industry-standard surface-measurement tools (stylus profilometry, 3D microscopy, and scanning white-light interferometry), the RMS height showed no time-dependent changes at all.
3. The inability of conventional techniques to measure these topography changes was attributed to two factors:
    a. The large surface slopes, cavities, and overhangs associated with a typical as-built AM surface preclude accurate measurement with conventional techniques, causing larger-scale topography to be underreported.
    b. As-built AM surfaces have significant topography contributions across several, largely uncorrelated, length scales; such that significant changes in topography on one scale are completely hidden by the unchanging topography at larger scales.

We hope that by identifying challenges in the measurement of surface topography, this work advances the understanding of AM surface topography and how it should be measured, analyzed, and controlled.

ACKNOWLEDGEMENTS

This work was funded by the National Science Foundation under grant number CMMI-2400999. Work performed in the University of Pittsburgh Nanofabrication and Characterization Core Facility (RRID:SCR_05124) and services and instruments used in this project were graciously supported, in part, by the University of Pittsburgh.

DATA AVAILABILITY

All raw and processed data required to reproduce these findings is freely available and can be accessed via DOI.

REFERENCES

[1] S. Bukkapatnam, J. Mander, S. Paal, Z. Pei, L. Zeng, Workshop Report: NSF Workshop on Additive Manufacturing (3D Printing) for Civil Infrastructure Design and Construction, Arlington, Virginia, 2017.
[2] Energetics Inc., Measurement Science Roadmap for Metal-Based Additive Manufacturing, 2013.
[3] B. Blakey-Milner, P. Gradl, G. Snedden, M. Brooks, J. Pitot, E. Lopez, M. Leary, F. Berto, A. du Plessis, Metal additive manufacturing in aerospace: A review, Mater. Des. 209 (2021) 110008. https://doi.org/10.1016/j.matdes.2021.110008.
[4] C. Culmone, G. Smit, P. Breedveld, Additive manufacturing of medical instruments: A state-of-the-art review, Addit. Manuf. 27 (2019) 461–473. https://doi.org/10.1016/j.addma.2019.03.015.
[5] S. Suresh, Fatigue of Materials, 2nd ed., Cambridge University Press, Cambridge, 1998. https://doi.org/10.1017/CBO9780511806575.
[6] A.A.G. Bruzzone, H.L. Costa, P.M. Lonardo, D.A. Lucca, Advances in engineered surfaces for functional performance, CIRP Ann. 57 (2008) 750–769. https://doi.org/10.1016/j.cirp.2008.09.003.
[7] Y. Du, T. Mukherjee, N. Finch, A. De, T. DebRoy, High-throughput screening of surface roughness during additive manufacturing, J. Manuf. Process. 81 (2022) 65–77. https://doi.org/10.1016/j.jmapro.2022.06.049.
[8] J. Han, Z. Li, Y. Sun, F. Cheng, L. Zhu, Y. Zhang, Z. Zhang, J. Wu, J. Wang, Surface Roughness and Biocompatibility of Polycaprolactone Bone Scaffolds: An Energy-Density-Guided Parameter Optimization for Selective Laser Sintering, Front. Bioeng. Biotechnol. 10 (2022). https://doi.org/10.3389/fbioe.2022.888267.
[9] R.K. Leach, D. Bourell, S. Carmignato, A. Donmez, N. Senin, W. Dewulf, Geometrical metrology for metal additive manufacturing, CIRP Ann. 68 (2019) 677–700. https://doi.org/10.1016/j.cirp.2019.05.004.
[10] N. Senin, A. Thompson, R. Leach, Feature-based characterisation of signature topography in laser powder bed fusion of metals, Meas. Sci. Technol. 29 (2018) 045009. https://doi.org/10.1088/1361-6501/aa9e19.
[11] V. Chadha, N.C. Miller, R. Ding, K.E. Beschorner, T.D.B. Jacobs, Evaluating scanning electron microscopy for the measurement of small-scale topography, Surf. Topogr. Metrol. Prop. 12 (2024) 035010. https://doi.org/10.1088/2051-672X/ad49b9.
[12] S. Kalpakjian, S.R. Schmid, Manufacturing Engineering and Technology, 8th ed., Pearson Prentice Hall, 2006. https://www.pearson.com/en-us/subject-catalog/p/manufacturing-engineering-and-technology/P200000003217/9780135211427.
[13] P.J. DePond, G. Guss, S. Ly, N.P. Calta, D. Deane, S. Khairallah, M.J. Matthews, In situ measurements of layer roughness during laser powder bed fusion additive manufacturing using low coherence scanning interferometry, Mater. Des. 154 (2018) 347–359. https://doi.org/10.1016/j.matdes.2018.05.050.
[14] C.K.P. Vallabh, X. Zhao, Melt pool temperature measurement and monitoring during laser powder bed fusion based additive manufacturing via single-camera two-wavelength

imaging pyrometry (STWIP), J. Manuf. Process. 79 (2022) 486–500. https://doi.org/10.1016/j.jmapro.2022.04.058.

[15] F. Cabanettes, A. Joubert, G. Chardon, V. Dumas, J. Rech, C. Grosjean, Z. Dimkovski, Topography of as built surfaces generated in metal additive manufacturing: A multi scale analysis from form to roughness, Precis. Eng. 52 (2018) 249–265. https://doi.org/10.1016/j.precisioneng.2018.01.002.

[16] S. Jamiolahmadi, A. Barari, Surface Topography of Additive Manufacturing Parts Using a Finite Difference Approach, J. Manuf. Sci. Eng. 136 (2014). https://doi.org/10.1115/1.4028585.

[17] A. Townsend, N. Senin, L. Blunt, R.K. Leach, J.S. Taylor, Surface texture metrology for metal additive manufacturing: a review, Precis. Eng. 46 (2016) 34–47. https://doi.org/10.1016/J.PRECISIONENG.2016.06.001.

[18] C.K. Stimpson, J.C. Snyder, K.A. Thole, D. Mongillo, Roughness Effects on Flow and Heat Transfer for Additively Manufactured Channels, J. Turbomach. 138 (2016). https://doi.org/10.1115/1.4032167.

[19] J.C. Snyder, C.K. Stimpson, K.A. Thole, D.J. Mongillo, Build Direction Effects on Microchannel Tolerance and Surface Roughness, J. Mech. Des. 137 (2015). https://doi.org/10.1115/1.4031071.

[20] T.D.B. Jacobs, L. Pastewka, Guest Editors, Surface topography as a material parameter, MRS Bull. 47 (2022) 1205–1210. https://doi.org/10.1557/s43577-022-00465-5.

[21] H.L. Costa, F.J. Profito, X. Zhang, K.A. Thole, Optimizing the surface of manufactured components for friction, adhesion, and convective heat transfer, MRS Bull. 47 (2022) 1247–1259. https://doi.org/10.1557/s43577-022-00467-3.

[22] A. Mostafaei, S.H.V.R. Neelapu, C. Kisailus, L.M. Nath, T.D.B. Jacobs, M. Chmielus, Characterizing surface finish and fatigue behavior in binder-jet 3D-printed nickel-based superalloy 625, Addit. Manuf. 24 (2018) 200–209. https://doi.org/10.1016/j.addma.2018.09.012.

[23] M. Atapour, X. Wang, M. Persson, I. Odnevall Wallinder, Y.S. Hedberg, Corrosion of Binder Jetting Additively Manufactured 316L Stainless Steel of Different Surface Finish, J. Electrochem. Soc. 167 (2020) 131503. https://doi.org/10.1149/1945-7111/abb6cd.

[24] A. Lores, N. Azurmendi, I. Agote, E. Espinosa, M.B. García-Blanco, A study of parameter and post-processing effects on surface quality improvement of Binder Jet 3D-printed Invar36 alloy parts, Prog. Addit. Manuf. 7 (2022) 917–930. https://doi.org/10.1007/s40964-022-00267-w.

[25] A.A. Vu, D.A. Burke, A. Bandyopadhyay, S. Bose, Effects of surface area and topography on 3D printed tricalcium phosphate scaffolds for bone grafting applications, Addit. Manuf. 39 (2021) 101870. https://doi.org/10.1016/j.addma.2021.101870.

[26] C. Zheng, A. Mostafaei, P.R. de Vecchis, I. Nettleship, M. Chmielus, Microstructure evolution for isothermal sintering of binder jet 3D printed alloy 625 above and below the solidus temperature, Addit. Manuf. 47 (2021) 102276. https://doi.org/10.1016/j.addma.2021.102276.

[27] W. Du, J. Hayes, K. Myers, B. Barua, W. Yu, D. Singh, Development of a High-Temperature Inconel 625 heat exchanger by model design and binder jetting additive manufacturing, Mater. Des. (2024) 113333. https://doi.org/10.1016/j.matdes.2024.113333.

[28] C. Zheng, I. Nettleship, M. Chmielus, A Novel Two-Step, Transient Liquid Phase Sintering Process for Densification of Binder-Jet 3D Printed Superalloys, Metall. Mater. Trans. A 55 (2024) 4318–4322. https://doi.org/10.1007/s11661-024-07584-5.
[29] A.M. Gokhale, Quantitative Characterization and Representation of Global Microstructural Geometry, (2004). https://doi.org/10.31399/asm.hb.v09.a0003759.
[30] E.L. Church, P.Z. Takacs, Instrumental Effects In Surface Finish Measurement, in: Surf. Meas. Charact., SPIE, 1989: pp. 46–55. https://doi.org/10.1117/12.949154.
[31] E.L. Church, P.Z. Takacs, Effects of the nonvanishing tip size in mechanical profile measurements, in: Opt. Test. Metrol. III Recent Adv. Ind. Opt. Insp., SPIE, 1991: pp. 504–514. https://doi.org/10.1117/12.51099.
[32] Principles of white-light interferometry to Michelson, (n.d.). https://www.polytec.com/us/surface-metrology/technology/white-light-interferometry (accessed January 15, 2025).
[33] N. Feiner-Gracia, S. Pujals, P. Delcanale, L. Albertazzi, 15 - Advanced Optical Microscopy Techniques for the Investigation of Cell-Nanoparticle Interactions, in: G. Ciofani (Ed.), Smart Nanoparticles Biomed., Elsevier, 2018: pp. 219–236. https://doi.org/10.1016/B978-0-12-814156-4.00015-X.
[34] R. Ding, A. Gujrati, M.M. Pendolino, K.E. Beschorner, T.D.B. Jacobs, Going Beyond Traditional Roughness Metrics for Floor Tiles: Measuring Topography Down to the Nanoscale, Tribol. Lett. 69 (2021) 92. https://doi.org/10.1007/s11249-021-01460-8.
[35] T.D.B. Jacobs, R.W. Carpick, Nanoscale wear as a stress-assisted chemical reaction, Nat. Nanotechnol. 8 (2013) 108–112. https://doi.org/10.1038/nnano.2012.255.
[36] T.D.B. Jacobs, K.E. Ryan, P.L. Keating, D.S. Grierson, J.A. Lefever, K.T. Turner, J.A. Harrison, R.W. Carpick, The Effect of Atomic-Scale Roughness on the Adhesion of Nanoscale Asperities: A Combined Simulation and Experimental Investigation, Tribol. Lett. 50 (2013) 81–93. https://doi.org/10.1007/s11249-012-0097-3.
[37] T.D.B. Jacobs, G.E. Wabiszewski, A.J. Goodman, R.W. Carpick, Characterizing nanoscale scanning probes using electron microscopy: A novel fixture and a practical guide, Rev. Sci. Instrum. 87 (2016) 013703. https://doi.org/10.1063/1.4937810.
[38] M.C. Röttger, A. Sanner, L.A. Thimons, T. Junge, A. Gujrati, J.M. Monti, W.G. Nöhring, T.D.B. Jacobs, L. Pastewka, Contact.engineering—Create, analyze and publish digital surface twins from topography measurements across many scales, Surf. Topogr. Metrol. Prop. 10 (2022) 035032. https://doi.org/10.1088/2051-672X/AC860A.
[39] A. Sanner, W.G. Nöhring, L.A. Thimons, T.D.B. Jacobs, L. Pastewka, Scale-dependent roughness parameters for topography analysis, Appl. Surf. Sci. Adv. 7 (2022) 100190. https://doi.org/10.1016/j.apsadv.2021.100190.
[40] ASME B46.1: Surface Texture (Surface Roughness, Waviness, and Lay), (2019).
[41] ISO 21920 - 2021: Geometrical product specifications (GPS) Surface texture: Profile, (2021).
[42] T. Jacobs, T. Junge, L. Pastewka, Quantitative characterization of surface topography using spectral analysis, Surf. Topogr. Metrol. Prop. 5 (2017) 013001. https://doi.org/10.1088/2051-672X/aa51f8.
[43] A. Cabo Rios, E. Hryha, E. Olevsky, P. Harlin, Sintering anisotropy of binder jetted 316L stainless steel: Part II – microstructure evolution during sintering, Powder Metall. 65 (2022) 283–295. https://doi.org/10.1080/00325899.2021.2020486.

[44] P.C. Searson, R. Li, K. Sieradzki, Surface Diffusion in the Solid-on-Solid Model, Phys. Rev. Lett. 74 (1995) 1395–1398. https://doi.org/10.1103/PhysRevLett.74.1395.